Journal of Materials Chemistry A

Accepted Manuscript

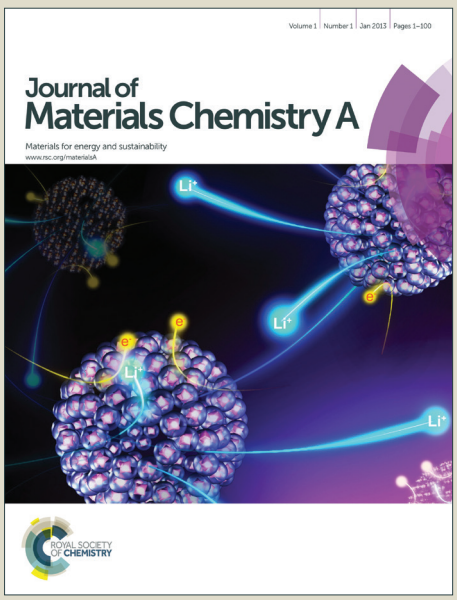

ROYAL SOCIETY OF CHEMISTRY

www.rsc.org/materialsA

Homogeneous core–shell $NiCo_2S_4$ nanostructure supported on nickel foam for supercapacitors

Wei Kong,[a] Chenchen Lu,[a] Wu Zhang[a,*], Jun Pu,[b] and Zhenghua Wang[†,a]

[a]*Key Laboratory of Functional Molecular Solids, Ministry of Education, College of Chemistry and Materials Science, Anhui Normal University, Wuhu 241000, P. R. China*

[b] *Suzhou Institute of Nanotech and Nanobionics, Chinese Academy of Sciences, 398 Ruoshui Road, Suzhou Industry Park, Suzhou 215123, P. R. China*

**Corresponding author. Tel.: +86-553-3869303; Fax: +86-553-3869302; E-mail: zhangwu@mail.ahnu.edu.cn (W. Zhang), zhwang@mail.ahnu.edu.cn (Z. Wang).*

Abstract: In this study, we report the fabrication of $NiCo_2S_4$ with a homogeneous core–shell nanostructure in which $NiCo_2S_4$ nanotubes are wraped by $NiCo_2S_4$ nanosheets. The core–shell structured $NiCo_2S_4$ were in situ grown on nickel foam and can be directly applied as supercapacitor electrode. Electrochemial tests demonstrate that the $NiCo_2S_4$ electrode achieved a high specific capacitance of 1948 mF cm^{-2} at a current density of 1 mA cm^{-2}, a good rate capability, and an excellent cycling stability. The outstanding performance of the $NiCo_2S_4$ electrode can be attributed to the core–shell architecture with good mechanical and electrical contact, rich redox reactions, as well as high transport rate for both electrolyte ions and electrons. By applying the $NiCo_2S_4$ as the positive electrode and porous carbon as the negative electrode, an asymmetric supercapacitor device was fabricated and exhibited an excellent electrochemical performance. These results demonstrate that the homogeneous core–shell $NiCo_2S_4$ nanostructure is promising for supercapacitor applications.

Keywords: $NiCo_2S_4$, core–shell structure, hydrothermal synthesis, pseudocapacitor, asymmetric supercapacitor

1. Introduction

Supercapacitors, also called electrochemical capacitors, is a new type of energy storage equipment which bridge the gap between conventional dielectric capacitors and rechargeable batteries.[1–5] Supercapacitors have attracted numerous attentions due to their high power density, excellent reversibility, high capacity, long cycle life, and so forth.[6–10] Supercapacitors can be divided into two different types in terms of the charge–storage mechanism, one is electrical double layer capacitors (EDLCs) which is dominated by electrostatic charge diffusion and accumulation at the interface of the electrode and electrolyte, the other is pseudocapacitors (also called redox electrochemical capacitors) which is mainly dominated by reversible fast surface Faradaic redox reactions. Carbon-based materials, such as activated carbon,[11,12] carbon nanotubes[13,14] and graphene[15,16] are usually used for EDLCs. While transition metal oxides such as RuO_2,[17] MnO_2,[18] NiO,[19] Co_3O_4[20] and $ZnCo_2O_4$[21] are usually used for pseudocapacitors. However, in spite of these attracting characteristics, the limited energy density of EDLCs and pseudocapacitors becomes a major hurdle for their implementation in practical applications. For example, in order to power electric vehicles, supercapacitors should have an energy density that comparable to lead-acid batteries (23–28 Wh kg^{-1}).[22] Nevertheless, the current commercial supercapacitors have an unsatisfactory energy density of less than 10 Wh kg^{-1}.[23] Therefore, the improvement of energy density without compromising the power density, cycling stability and cost effectiveness is a primary focus in the development of supercapacitors.

Recently, transition metal sulfides have been tried as a new type of electrode material for supercapacitors. Compare to the low capacity of carbon materials, the high cost of RuO_2, and the poor cycle performance of conducting polymers, transition metal sulfides have achieved many excellent electrochemical properties. For example, flower-like CoS hierarchitectures showed a specific capacitance of 586 F g^{-1} at a current density of 1 A g^{-1};[24] flower-like beta-NiS exhibited a capacitance of 857.76 F g^{-1} at a current density of 2 A g^{-1};[25] MoS_2 achieved a capacitance of 553.7 F g^{-1} at a current density of 1 A g^{-1}.[26] Similar to Ni–Co binary oxides, Ni–Co binary sulfides may possess higher electrochemical activity than nickel sulfides and cobalt sulfides based on their richer redox reactions. Various nanostructures of $NiCo_2S_4$, such as nanotubes,[27,28] nanowires,[29,30] hollow hexagonal nanoplates,[31] nanosheets,[32] three-dimensional nanonetworks,[33] urchin-like nanostructures,[31] and cubic-like microstructures[35] have been reported. Better electrochemical performances of $NiCo_2S_4$ can be expected by elaborately designing various ion diffusion favored structures, such as the core–shell structure.

In this work, we report the fabrication of $NiCo_2S_4$ with a novel homogeneous core–shell nanostructure in which $NiCo_2S_4$ nanotubes are wraped by $NiCo_2S_4$ nanosheets. The core–shell structured $NiCo_2S_4$ were directly grown on nickel foam substrate, which avoided the using of non-conducting organic binders during the fabrication of the electrode. The as-fabricated $NiCo_2S_4$ sample shows ultrahigh specific capacitances, outstanding capacitance retention at high-rates and excellent cycling stability. Furthermore, an asymmetric capacitor device was fabricated by

using the $NiCo_2S_4$ sample as the positive electrode and porous carbon as the negative electrode. The as-fabricated asymmetric supercapacitor device exhibits high specific energy and power density. The results suggest that the core–shell structured $NiCo_2S_4$ can act as high performance electrode material for supercapacitor applications.

2. Experimental section

2.1 Materials. Cobalt chloride hexahydrate ($CoCl_2·6H_2O$), nickel chloride hexahydrate ($NiCl_2·6H_2O$), urea ($CO(NH_2)_2$), sodium sulfide ($Na_2S·9H_2O$), potassium hydroide (KOH), hydrochloric acid (HCl) and absolute ethanol were commercially available from Sinopharm Chemical Reagent Co. in analytical grade and were used without further purification.

2.2 Growth of $NiCo_2S_4$ on nickel foam. The growth of $NiCo_2S_4$ on nickel foam was realized through a two-step hydrothermal method. In a typical procedure, $CoCl_2·6H_2O$ (0.095 g, 0.4 mmol), $NiCl_2·6H_2O$ (0.048 g, 0.2 mmol) and $CO(NH_2)_2$ (0.3 g, 5 mmol) were added into 30 mL deionized water under stirring to obtain a light pink solution. A piece of nickel foam (2 cm × 2 cm) was treated with 6 M HCl for 10 min to remove the oxide layer and then washed thoroughly with deionized water. The above solution and the nickel foam were transferred into a Teflon-lined stainless-steel autoclave with a capacity of 50 mL, and heated at 100 °C for 8 h. After being cooled to room temperature naturally, the pink precursor loaded nickel foam was collected, rinsed with deionized water several times for further use.

In the next step, $Na_2S·9H_2O$ (0.48 g, 2 mmol) was dissolved in 40 mL distilled water to form a clear solution. Then the solution and the precursor loaded nickel foam were transferred into a Teflon-lined stainless-steel autoclave and heated at 110 °C for 4 h. After being cooled to room temperature naturally, the nickel foam was collected, rinsed with deionized water and absolute ethanol several times each, and dried under vacuum at 50 °C for 2 h. Black product can be seen evenly loaded on nickel foam (Figure S1). The mass loading of $NiCo_2S_4$ on nickel foam is about 1.0 mg cm^{-2}.

2.3 Characterization. X-ray powder diffraction (XRD) patterns were obtained on a Shimadzu XRD 6000 X-ray diffractometer with Cu Kα radiation. X-ray photoelectron spectroscopies (XPS) were performed on an ESCALab MKII X-ray photoelectron spectrometer with Al Kα radiation. Scanning electron microscopy (SEM) images and energy dispersive X-ray spectra (EDX) were captured on a Hitachi S-4800 scanning electron microscope. Transmission electron microscopy (TEM) images, high-resolution TEM (HRTEM) images were obtained on a FEI Tecnai G^2 20 transmission electron microscope equipped with an EDX spectrometer. Elemental mappings were obtained on a JEOL JEM-2100F transmission electron microscope equipped with an EDX spectrometer. N_2 adsorption measurements were tested on a Micromeritics ASAP 2020 M+C volumetric adsorption equipment at 77 K using Barrett-Emmett-Teller (BET) calculations for surface area.

2.4 Electrochemical measurements. For the three-electrode electrochemical measurements, the $NiCo_2S_4$ loaded nickel foam (1.0 cm × 1.0 cm) directly acted as the working electrode, a platinum plate and an Hg/HgO electrode acted as the counter and

reference electrodes, respectively. A 6 M KOH aqueous solution acted as the electrolyte.

For the asymmetric supercapacitor device tests, the $NiCo_2S_4$ loaded nickel foam (2.0 cm × 2.0 cm) directly acted as the positive electrode, porous carbon prepared according to literature report served as the negative electrode material.[36] The negative electrode was prepared by mixing porous carbon, acetylene black and poly-tetrafluoroethylene (PTFE) in a mass ratio of 80:15:5 to obtain a slurry. Then the slurry was pressed onto a piece of nickel foam (2.0 cm × 2.0 cm) and dried at 70 ℃ for 12 h. The positive and negative electrodes were put together and separated by a piece of cellulose paper separator that has been soaked with 6 M KOH aqueous solution.

3. Results and discussion

3.1. Characterization of homogeneous core–shell $NiCo_2S_4$ nanostructure. The composition and purity of the as-obtained samples are analyzed by XRD technique. The precursor is composed of $Ni_2(OH)_2CO_3 \cdot H_2O$ and $Co(CO_3)_{0.5}(OH)_{0.11} \cdot H_2O$, as we have previsouly reported (Figure S2a).[33] Figure 1 shows a typical XRD pattern of the $NiCo_2S_4$ sample obtained through hydrothermal treating the precursor in Na_2S solution, the diffraction peaks located at 31.4°, 38.1°, 50.3° and 55.1° can be indexed to the (311), (400), (511) and (440) planes of cubic phase $NiCo_2S_4$ (JCPDS no. 43-1477), and the strong peaks at 44.4°, 52.0° and 76.6° can be assigned to nickel foam substrate. A weak peak at 29.8° may correspond to Co_9S_8 (JCPDS 86-2273), and

another weak peak at about 22.0° may be attributed to Ni_3S_2 (JCPDS 85-0775). The results reveal that the as-obtained sample is mainly $NiCo_2S_4$.

--------Figure 1--------

The chemical bonding states of each element on the surface of $NiCo_2S_4$ sample are evaluated by XPS technique. Figure 2a shows a survey XPS spectrum of the $NiCo_2S_4$ sample in the range of 0–1000 eV. The peaks at 169.7, 781.5 and 855.7 eV correspond to S 2p, Co 2p and Ni 2p, respectively, indicating the existence of S, Co and Ni elements in the as-prepared sample. The C (as reference) and O elements are due to exposure to the air. The Co 2p and Ni 2p XPS spectra were computer fitted using a Gaussian fitting method considering two spin–orbit doublets and two shakeup satellites (marked as "Sat."). Figure 2b shows the Co 2p XPS spectrum, the strong peaks at 781.2 eV for Co $2p_{3/2}$ and 796.5 eV for Co $2p_{1/2}$ are demonstrated, suggesting both Co^{3+} and Co^{2+} in the $NiCo_2S_4$ sample. The weak satellite peaks indicate that the majority of cobalt is Co^{3+}.[37] Figure 2c depicts the Ni 2p XPS spectrum, the peaks at 855.6 eV for Ni $2p_{3/2}$ and 873.1 eV for Ni $2p_{1/2}$ suggests the existence of both Ni^{2+} and Ni^{3+}. The intense satellite peaks indicate that Ni^{2+} is the majority.[38] The S 2p XPS spectrum is shown in Figure 2d, the binding energies at 163.6 and 162.1 eV correspond to S $2p_{1/2}$ and S $2p_{3/2}$, respectively.[39,40]

--------Figure 2--------

The morphology of the $NiCo_2S_4$ loaded on nickel foam is firstly examined with SEM. Figure 3a illustrates a representative low-magnification SEM image of the nickel foam, indicating that the nickel foam is uniformly covered with a layer of

$NiCo_2S_4$. Magnified views of the $NiCo_2S_4$ (Figure 3b,c) show the presence of many rod-like nanomaterials, these rod-like nanomaterials are interconnected to each other and formed a 3D hierarchical structure. Further magnified view of the $NiCo_2S_4$ (Figure 3d) indicates that the rod-like $NiCo_2S_4$ is wrapped in thin nanosheets.

--------Figure 3--------

To better illustrate the morphology of the as-obtained product, the $NiCo_2S_4$ sample was separated from nickel foam by ultrasonication, and then was characterized by TEM. Figure 4a shows a representative TEM image of the $NiCo_2S_4$ sample, indicating that the rod-like nanomaterials are nanotubes indeed, and are wrapped with thin nanosheets, forming a core–shell structure. Figure 4b shows a clear view of the nanosheets wrapped nanotubes. The nanotube has a diameter of about 60 nm, and a wall thickness of about 10 nm. The nanotube is polycrystalline and is consisted of numerous interconnected nanoparticles. HRTEM image of the $NiCo_2S_4$ sample is shown in Figure 4c, the lattice fringes in the HRTEM image were calculated to be 0.24 nm in the nanotube and 0.28 nm in the nanosheet, which matches with the (400) and (311) lattice planes of $NiCo_2S_4$, respectively. This result confirms that both the nanotube and the nanosheet are $NiCo_2S_4$. An EDX spectrum of the $NiCo_2S_4$ sample is shown in Figure 4d, the peaks of S, Co, Ni elements are clearly observed, consistent with the elemental composition of $NiCo_2S_4$. The element ratio of Ni, Co and S is 13.5:26.4:40.6, which matches with the formula of $NiCo_2S_4$. The presence of O element may be due to the partial surface oxidation of the sample.

--------Figure 4--------

The BET surface area of the core–shell structured $NiCo_2S_4$ sample was determined by N_2 adsorption-desorption isotherms, and the corresponding pore size distributions were calculated by Barrett-Joyner-Halenda (BJH) method, as displayed in Figure S3. The isotherm (Figure S3a) exhibit characteristics of type-IV isotherms with a pronounced hysteresis loop according to the IUPAC classification. A BET surface area of about 25.6 $m^2 g^{-1}$ was calculated. Figure S3b shows the corresponding BJH pore size distribution curves of the samples, indicating that the pores of the $NiCo_2S_4$ samples mainly locate in 5–50 nm.

Figure 5 reveals elemental mappings of the homogeneous core–shell $NiCo_2S_4$ nanostructure. The Ni, Co, and S elements are uniformly and continuously distributed in both the nanotube and the nanosheet. As the nanosheet is very thin, the density of elements in the nanosheets is lower than that in the nanotube. The elemental mappings results further confirm that both the nanotube and the nanosheet are $NiCo_2S_4$.

--------Figure 5--------

3.2 Formation process and influencing factors. The $NiCo_2S_4$ sample was obtained through hydrothermal treating the precursor in Na_2S solution. The precursor served as a sacrificial hard template for the preparation of the $NiCo_2S_4$ sample. As indicated by SEM and TEM observations (Figure S2b,c), the precursor is composed of many uniform nanorods. Under hydrothermal condition, the reaction between the precursor and S^{2-} was occurred on the surfaces of the precursor nanorods, which result in the formation of hollow structured product due to the Kirkendall effect.[37] Figure 6 shows time dependent products obtained at 110 °C, which illustrates the

growth process of the core–shell structured $NiCo_2S_4$. After 1 h, some nanoparticles appear on the core, as shown in Figure 6a. With the reaction proceeded, more nanoparticles appear on the core (Figure 6b). The product obtained after 3 h starts take on core–shell structure (Figure 6c). After 4 h, $NiCo_2S_4$ core–shell nanostructure with nanosheets wraped nanotubes was obtained (Figure 6d).

--------Figure 6--------

The reacting temperature of the reaction between the precursor and Na_2S solution has significant influence on the morphology of the final product. Figure 7 shows the $NiCo_2S_4$ products obtained at different reacting temperatures. When the temperature is 110 °C, homogeneous core–shell structured $NiCo_2S_4$ was obtained (Figure 7b). However, at higher (e.g. 120 °C) and lower (e.g. 100 °C) temperature, the core–shell structure could not be obtained. The formation mechanism of the homogeneous core–shell structure is not very clear and needs further research.

--------Figure 7--------

3.3. Electrochemical performance of the $NiCo_2S_4$ electrode. The core–shell structured $NiCo_2S_4$ loaded nickel foam was directly used as electrode for supercapacitor and its electrochemical performances were tested by cyclic voltammetry (CV) and galvanostatic charge–discharge technique in a three-electrode system. Figure 8a shows representative CV curves of the electrode in the potential window of 0 to 0.7 V with various sweeping rates ranging from 10 to 100 mV s^{-1}. According to these curves, it is clear that two pairs of redox peaks are visible in the CV curves, suggesting the pseudocapacitive characteristics of the $NiCo_2S_4$ active

material. With the increase of sweep rates, the current density increases, and the position of anodic and cathodic peaks shifts to more positive and negative directions, respectively. The mechanism of electrochemical reactions can be attributed to the reversible Faradaic redox processes of $Co^{2+}/Co^{3+}/Co^{4+}$ and Ni^{2+}/ Ni^{3+} based on the following reactions:[34]

$$CoS + OH^- \leftrightarrow CoSOH + e^- \quad (1)$$

$$CoSOH + OH^- \leftrightarrow CoSO + H_2O + e^- \quad (2)$$

$$NiS + OH^- \leftrightarrow NiSOH + e^- \quad (3)$$

A comparison of the CV curves of pure nickel foam and the $NiCo_2S_4$ supported nickel foam is shown in Figure 8b, the CV curve of pure nickel foam is almost a straight line, suggesting that the capacitance contributed from nickel foam can be ignored.

Galvanostatic charge–discharge measurements were conducted in a potential window of 0 to 0.5 V at various current densities ranging from 1 to 20 mA cm^{-2}. Figure 8c shows representative charge–discharge curves with various current densities. Clearly, the curves at low current densities show two obvious platforms, which correspond to the redox reactions. The capacitances of the electrode can be evaluated according to the following equations:[41]

$$C_s = \frac{I \times \Delta t}{m \times \Delta V} \quad (4)$$

$$C_a = \frac{I \times \Delta t}{S \times \Delta V} \quad (5)$$

where C_s (F g^{-1}) is the specific capacitance, C_a (mF cm^{-2}) is the areal capacitance, I (A) is the current during the discharge process, S (cm^2) is the geometrical area of the electrode, Δt (s) is the discharge time, ΔV (V) is the potential window and m (g) is the

mass of the active materials. At a current density of 1 mA cm^{-2} (1 A g^{-1}), the electrode demonstrates an areal capacitance of 1948 mF cm^{-2} (specific capacitance of 1948 F g^{-1}). It is worthy noting that the $NiCo_2S_4$ electrode demonstrates a remarkable areal capacitance of 1546 mF cm^{-2} even the current density is as high as 20 mA cm^{-2}, suggesting the good rate capacity of the $NiCo_2S_4$ sample (Figure 8d).

Electrochemical performances of the core–shell structured $NiCo_2S_4$ and $NiCo_2S_4$ nanotubes obtained at 120 °C was compared. Figure S4a shows CV curves of the two samples at a sweeping rate of 100 mV s^{-1}, from which we can learn that the core–shell structured $NiCo_2S_4$ sample has a larger integral area surrounded by CV curve. Figure S4b shows galvanostatic charge–discharge curves of the two samples at a current density of 2 mA cm^{-2}, the areal capacitance of $NiCo_2S_4$ nanotubes is 1260 mF cm^{-2}, which is obviously lower than that of the core–shell structured $NiCo_2S_4$ sample (1838 mF cm^{-2}). The better electrochemical performances of the core–shell structured $NiCo_2S_4$ can be attributed to its unique structure which can provide more active sites for electrochemical reactions.

Long cycling life is an important requirement for supercapacitors. Figure 8e shows the cycling performance of the $NiCo_2S_4$ electrode at a current density of 2 mA cm^{-2}. After 5000 successive cycles, there is still approximately 94% retention of the initial capacitance. The inset in Figure 8e displays the cycling performance of the $NiCo_2S_4$ electrode at various current densities. The capacitance of the $NiCo_2S_4$ electrode can still be retained after cycled at high current densities. These results indicate the excellent cycle stability of the $NiCo_2S_4$ electrode. SEM and TEM images

(Figure S5) of the $NiCo_2S_4$ electrode material after 5000 cycles show almost the same feature as those before cycling. Figure 8f displays the Nyquist plots of $NiCo_2S_4$ at the first cycle and after 100 cycles in the frequency range of 100 kHz to 0.01 Hz. The remarkably similar curves indicate the high stability of the electrode.

--------Figure 8--------

3.4. Electrochemical performance of the $NiCo_2S_4$//C asymmetric supercapacitor device. To further evaluate the $NiCo_2S_4$ electrode for practical application, an asymmetric supercapacitor device was fabricated by using the $NiCo_2S_4$ sample as the positive electrode, porous carbon as the negative electrode, and 6 M KOH aqueous solution as the electrolyte. The porous carbon was prepared according to literature report,[36] and it shows a specific capacitance of 252 F g^{-1} at a current density of 2 A g^{-1} (Figure S6). As for the supercapacitor device, the charges stored at the two electrodes are equal in magnitude. In order to gain good electrochemical performances, the mass ratio of the positive and negative electrode materials should follow the following equation:[41]

$$\frac{m_+}{m_-} = \frac{C_- \times \Delta E_-}{C_+ \times \Delta E_+} \qquad (6)$$

Where C_+ and C_- are the specific capacitances of the positive and negative electrodes, ΔE_- and ΔE_+ represent the potential window for the electrodes, and m_+ and m_- are the mass of electrode materials. The mass ratio of the positive and negative electrode materials is 0.27.

Figure 9a shows comparative CV curves of the positive and negative electrodes measured at a scan rate of 50 mV s^{-1} in three-electrode system. The $NiCo_2S_4$ electrode

can be operated within a potential window of 0 to 0.7 V, and the porous carbon electrode can be operated within a potential window of −1 to 0 V. Therefore, the asymmetric supercapacitor device can work on a voltage of 1.6 V. Figure 9b shows CV cures of the $NiCo_2S_4$//C asymmetric supercapacitor device at different voltage windows from 1 to 1.6 V at a scan rate of 50 mV s^{-1}. As expected, the stable electrochemical windows of the asymmetric supercapacitor device can be extended to 1.6 V. Figure 9c shows the CV cures of the $NiCo_2S_4$//C asymmetric supercapacitor device at different scan rates with a potential window of 0 to 1.6 V, these CV curves show electrical double layer capacitance and pseudocapacitance characteristics between porous carbon and $NiCo_2S_4$. In addition, the CV profiles do not have obvious distortion with increasing potential scan rates, even at a high scan rate of 100 mV s^{-1}, indicating the desirable fast charge–discharge property of the asymmetric supercapacitor device. Galvanostatic charge–discharge curves of the $NiCo_2S_4$//C asymmetric supercapacitor device at a serious of current densities are demonstrated in figure 9d, the specific capacitance increase with the decrease of current density, the specific capacitances are 341, 261, 223, 192, 160 and 117 mF cm^{-2} at current densities of 1, 2, 4, 8, 16 and 32 mA cm^{-2}.

The cycling performances of $NiCo_2S_4$//C asymmetric supercapacitor device was examined at a current density of 5 mA cm^{-2}, and the results are shown in Figure 9e. The capacitance increases to 490 mF cm^{-2} in the first one hundred cycles, which may due to the activation of active electrode material.[30] Then the capacitance starts to decrease. After 5000 cycles, a capacitance of 375 mF cm^{-2} is still retained, indicating

the good cycle stability of the asymmetric supercapacitor device. Figure 9f presents comparative Ragone plots of the asymmetric supercapacitor device in terms of gravimetric performances measured at different charge–discharge current densities. The power density and energy density of the asymmetric supercapacitor device were calculated by the following equations:[41]

$$E = \frac{1}{2} C \Delta V^2 \quad (7)$$

$$P = \frac{E}{\Delta t} \quad (8)$$

where C represents the specific capacitance of the asymmetric supercapacitor, ΔV refers to the operating voltage of the device, Δt is the discharge time, E is the energy density and P is the power density. The $NiCo_2S_4$//C asymmetric supercapacitor device displays a high energy density of 22.8 W h kg^{-1} at a current density of 1 mA cm^{-2}, and the corresponding power density is 0.16 kW kg^{-1}. When the current density increased to 16 mA cm^{-2}, the power density can reach a high value of 2.47 kW kg^{-1}, while the energy density can be still maintained at 10.6 W h kg^{-1}. The high energy density can be attributed to the high specific capacitance and the wide voltage window. Moreover, the performance of the $NiCo_2S_4$//C asymmetric supercapacitor can be comparable to or even better than other asymmetric supercapacitor devices.[42–46] Furthermore, two asymmetric supercapacitor devices were assembled in series, and the devices are charged to 3.0 V in about 10 s. After that, a red-light LED is lighted by the devices (Figure S7), and the LED continuously worked for 270 seconds. This result demonstrates the remarkable performance of the asymmetric supercapacitors devices and the electroactive material in practical applications.

The superior supercapacitive performance of the core–shell structured $NiCo_2S_4$ can be ascribed to the following aspects: (1) The $NiCo_2S_4$ is directly grown on nickel foam, which can gain good mechanical and electrical contact with the nickel foam. (2) The core–shell structure possesses large surface area, which provide numerous of electroactive sites for ions adsorption and Faradaic redox reactions. (3) The $NiCo_2S_4$ sample possess higher conductivity and richer redox reaction than the oxides. All of the aspects are beneficial for improving the supercapacitive performances.

--------Figure 9--------

4. Conclusions

In summary, homogeneous core–shell $NiCo_2S_4$ nanostructure supported on nickel foam were successfully fabricated by a facial two-step hydrothermal route. The $NiCo_2S_4$ loaded nickel foam can be directly used as supercapacitor electrode. Electrochemical tests show that the $NiCo_2S_4$ electrode exhibits an ultrahigh specific capacitance, as well as good rate capability and cycle performance. An asymmetric supercapacitor device based on the $NiCo_2S_4$ as positive electrode, porous carbon as negative electrode and KOH as electrolyte can work steadily on a voltage of 1.6 V, and can deliver a high energy density of 22.8 W h kg^{-1}at 1 mA cm^{-2} as well as a high power density of 2.47 kW kg^{-1} at 16 mA cm^{-2}. The homogeneous core–shell $NiCo_2S_4$ nanostructure could be considered as a potential electrode material for high energy density storage supercapacitors.

Acknowledgment

Financial support form the National Natural Science Foundation of China (NSFC no. 21171006, 21272006) is gratefully acknowledged.

Notes and References

† Electronic Supplementary Information (ESI) available: Photographs of the nickel foam, precursor loaded nickel foam and $NiCo_2S_4$ loaded nickel foam; XRD, SEM and TEM images of the precursor; N_2 adoption and desorption isotherm and BJH pore size distributions; Typical CV and charge–discharge curves of the porous carbon and $NiCo_2S_4$ nanotubes; SEM and TEM images of $NiCo_2S_4$ sample after 5000 cycles; Photograph of a red LED lighted up by the device.

(1) J. M. Tarascon and M. Armand, *Nature,* 2001, **414**, 359.

(2) M. Winter and R. J. Brodd, *Chem. Rev.,* 2004, **104**, 4245.

(3) J. R. Miller and P. Simon, *Science,* 2008, **321**, 651.

(4) Z. J. Fan, J. Yan, L. J. Zhi, Q. Zhang, T. Wei, J. Feng, M. L. Zhang, W. Z. Qian and F. Wei, *Adv. Mater.*, 2010, **22**, 3723.

(5) X. F. Wang, B. Liu, Q. F. Wang, W. F. Song, X. J. Hou, D. Chen, Y. B. Cheng and G. Z. Shen, *Adv. Mater.*, 2013, **25**, 1479.

(6) P. Simon and Y. Gogotsi, *Nat. Mater.*, 2008, **7**, 845.

(7) C. Z. Yuan, L. Yang, L. R. Hou, L. F. Shen, X. G. Zhang and X. W. Lou, *Energy Environ. Sci.,* 2012, **5**, 7883.

(8) C. Yuan, J. Li, L. Hou, X. Zhang, L. Shen and X. W. Lou, *Adv. Funct. Mater.*, 2012, **22**, 4592.

(9) J. P. Liu, J. Jiang, C. W. Cheng, H. X. Li, J. X. Zhang, H. Gong and H. J. Fan, *Adv. Mater.*, 2011, **23***,* 2076.

(10) L. F. Chen, Z. Y. Yu, J .J. Wang, Q. X. Li, Z. Q. Tan, Y. W. Zhu and S .H. Yu, *Nano Energy* 2015, **11**, 119.

(11) L. L. Zhang and X. S. Zhao, *Chem. Soc. Rev.*, 2009, **38**, 2520.

(12) X. Y. Chen, C. Chen, Z. J. Zhang and D. H. Xie, *J. Mater. Chem. A,* 2013, **1**, 7379.

(13) Z. Chen, Y. Yuan, H. H. Zhou, X. L. Wang, Z. H. Gan, F. S. Wang and Y. F. Lu, *Adv. Mater.*, 2014, **26**, 339.

(14) R. Yuksel, Z. Sarioba, A. Cirpan, P. Hiralal and H. E. Unalan, *ACS Appl. Mater. Interfaces,* 2014, **6**, 15434.

(15) Y. X. Xu, Z. Y. Lin, X. Q. Huang, Y. Wang, Y. Huang and X. F. Duan, *Adv. Mater.*, 2013, **25**, 5779.

(16) P. Chen, J. J. Yang, S. S. Li, Z. Wang, T. Y. Xiao, Y. H. Qian and S. H. Yu, *Nano Energy,* 2013, **2**, 249.

(17) N. Soin, S. S. Roy, S. K. Mitra, T. Thundat and J. A. McLaughlin, *J. Mater. Chem.,* 2012, **22**, 14944.

(18) H. Jiang, T. Zhao, J. Ma, C. Y. Yan and C. Z. Li, Chem. Commun., 2011, **47**, 1264.

(19) B. Wang, J. S. Chen, Z. Wang, S. Madhavi and X. W. Lou, *Adv. Energy Mater.*, 2012, **2**, 1188.

(20) R. Tummala, R. K. Guduru and P. S. Mohanty, *J. Power Sources,* 2012, **209**, 44.

(21) B. Liu, B. Y. Liu, Q. F. Wang, X. F. Wang, Q. Y. Xiang, D. Chen and G. Z. Shen, *ACS Appl. Mater. Interfaces,* 2013, **5**, 10011.

(22) N. Omar, M. Daowd, P. van den Bossche, O. Hegazy, J. Smekens, T. Coosemans and J. van Mierlo, *Energies,* 2012, **5**, 2952.

(23) J. Yan, Q. Wang, T. Wei abd Z. J. Fan, *Adv. Energy Mater.,* doi: 10.1002/aenm.201300816.

(24) F. L. Luo, J. Li, H. Y. Yuan and D. Xiao, *Electrochim. Acta,* 2014, **123**, 183.

(25) J. Q.Yang, X. C. Duan, Q. Qin and W. J. Zheng, *J. Mater. Chem. A,* 2013, **1**, 7880.

(26) G. F. Ma, H. Peng, J. J. Mu, H. H. Huang, X. Z. Zhou and Z. Q. Lei, *J. Power Sources,* 2013, **229**, 72.

(27) H. Z. Wan, J. J. Jiang, J. W. Yu, K. Xu, L. Miao, L. Zhang, H. C. Chen and Y. J. Ruan, *CrystEngComm,* 2013, **15**, 7649.

(28) H. C. Chen, J. J. Jiang, L. Zhang, D. D. Xia, Y. D. Zhao, D. Q. Guo, T. Qi and H. Z. Wan, *J. Power Sources*, 2014, **254**, 249.

(29) Y. H. Li, L. J. Cao, L. Qiao, M. Zhou, Y. Yang, P. Xiao and Y. H. Zhang, *J. Mater. Chem. A,* 2014, **2**, 6540.

(30) R. J. Zou, Z. Y. Zhang, M. F. Yuen, J. Q. Hu, C. S. Lee and W. J. Zhang, *Sci. Rep.*, 2015, **5**, 7862.

(31) J. Pu, F. L. Cui, S. B. Chu, T. T. Wang, E. H. Sheng and Z. H. Wang, *ACS Sustainable Chem. Eng.,* 2014, **2**, 809.

(32) W. Chen, C. Xia and H. N. Alshareef, *ACS Nano,* 2014, **8**, 9531.

(33) Y. Liu, J. A. Zhang, S. P. Wang, K. X. Wang, Z. M. Chen and Q. Xu, *New J. Chem.*, 2014, **38**, 4045

(34) H. C. Chen, J. J. Jiang, L. Zhang, H. Z. Wan, T. Qi and D. D. Xia, *Nanoscale,* 2013, **5**, 8879.

(35) Y. F. Zhang, M. Z. Ma, J. Yang, C. C. Sun, H. Q. Su, W. Huang and X. C. Dong, *Nanoscale*, 2014, **6**, 9824.

(36) X. Y. Chen, C. Chen, Z. J. Zhang and D. H. Xie, *J. Mater. Chem. A,* 2013, **1**, 10903.

(37) J. Pu, T. T. Wang, H. Y. Wang, Y. Tong, C. C. Lu, W. Kong and Z. H. Wang, *ChemPlusChem,* 2014, **79**, 577.

(38) J. G. Kim, D. L. Pugmire, D. Battaglia and M. A. Langell, *Appl. Surf. Sci.,* 2000, **165**, 70.

(39) Q. H. Wang, L. F. Jiao, H. M. Du, Y. C. Si, Y. J. Wang and H. T. Yuan, *J. Mater. Chem.,* 2012, **22**, 21387.

(40) W. M. Du, Z. Y. Wang, Z. Q. Zhu, S. Hu, X. Y. Zhu, Y. F Shi, H. Pang and X. F. Qian, *J. Mater. Chem. A*, 2014, **2**, 9613.

(41) K. B. Xu, W. Y. Li, Q. Liu, B. Li, X. J. Liu, L. An, Z. G. Chen, R. J. Zou and J. Q. Hu, *J. Mater. Chem. A,* 2014, **2**, 4795.

(42) S. T. Senthilkumar and R. K. Selvan, *Phys. Chem. Chem. Phys.*, 2014, **16**, 15692.

(43) V. Aravindan, M. V. Reddy, S. Madhavi, S. G. Mhaisalkar, G. V. S. Rao and B. V. R. Chowdari, *J. Power Sources,* 2011,**196**, 8850.

(44) W. Hong, J. Q. Wang, P. W. Gong, J. F. Sun, L. Y. Niu, Z. G. Yang, Z. F. Wang and S. R. Yang, *J. Power Sources,* 2014, **270**, 516.

(45) W. D. Yu, W. R. Lin, X. F. Shao, Z. X. Hu, R. C. Li and D. S. Yuan, *J. Power Sources,* 2014, **272**, 137.

(46) D. W. Wang, F. Li and H. M. Cheng, *J. Power Sources,* 2008, **185**, 1563.

Figure captions

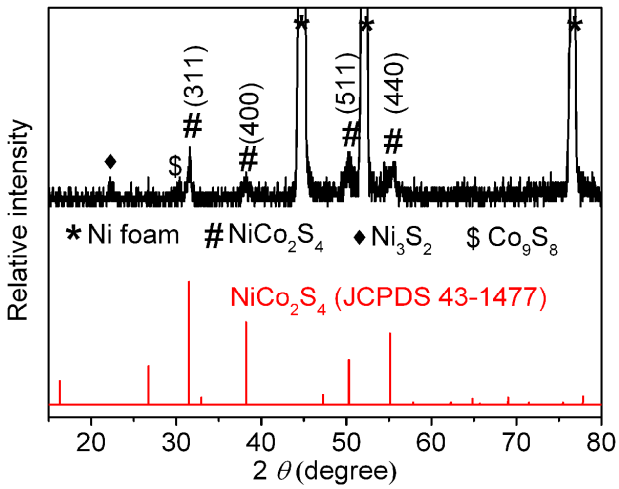

Figure 1. XRD pattern of $NiCo_2S_4$ supported on nickel foam.

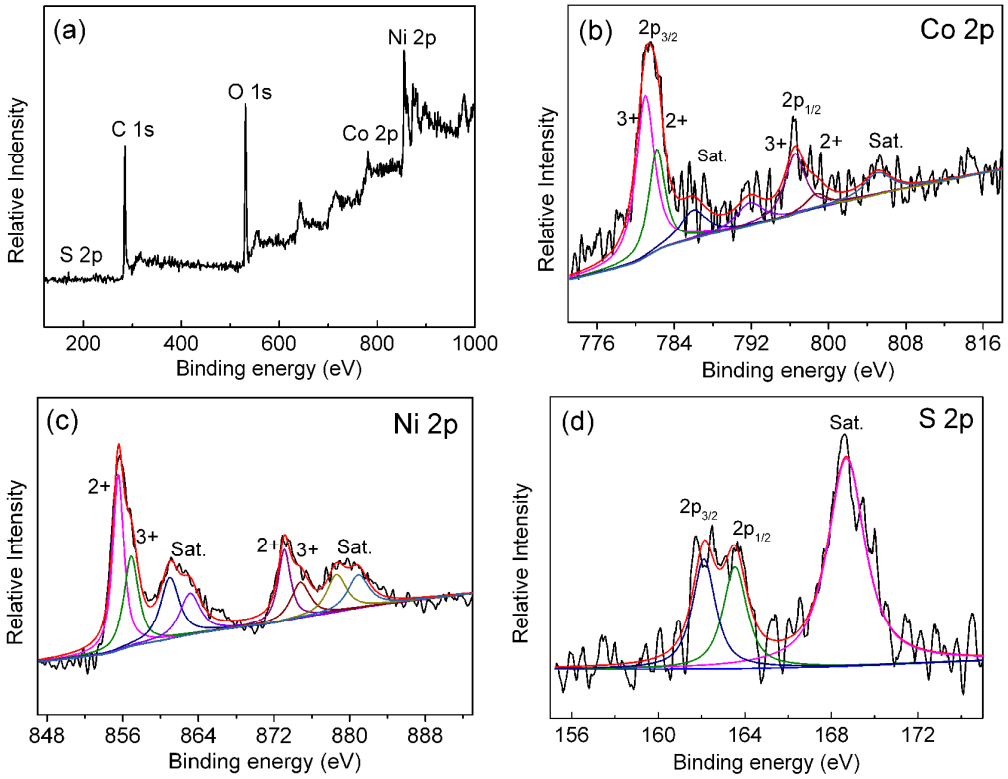

Figure 2. XPS spectra of the as-obtained $NiCo_2S_4$ sample: (a) survey, (b) Co 2p, (c) Ni 2p and (d) S 2p.

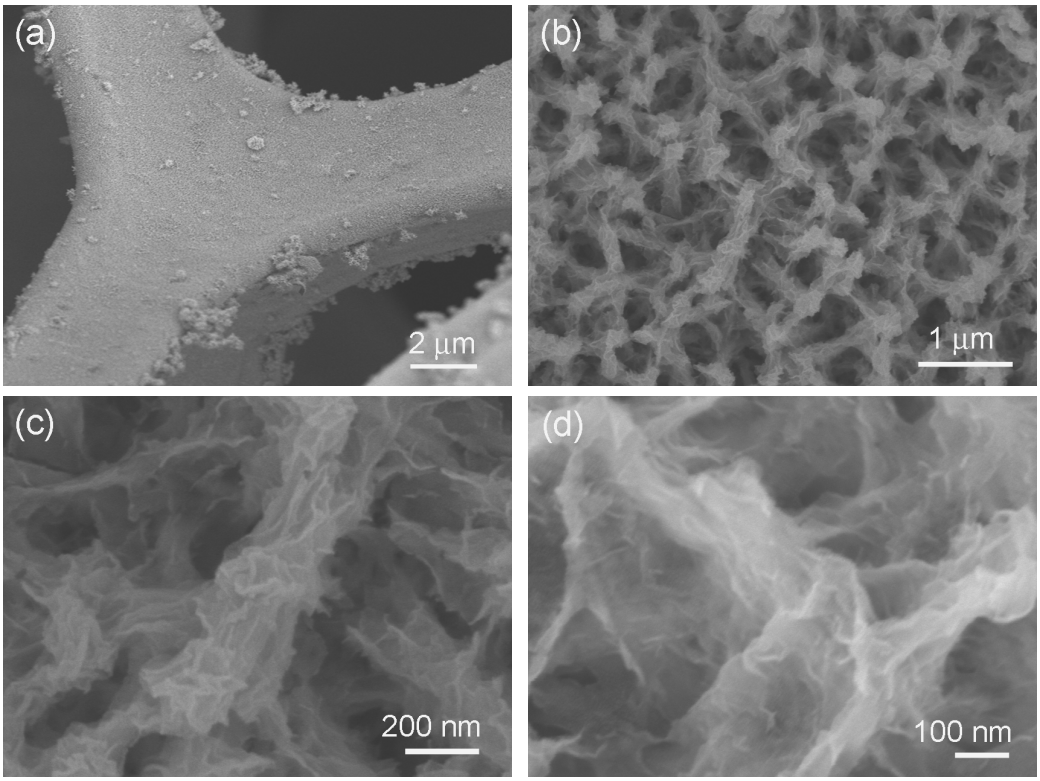

Figure 3. SEM images of the $NiCo_2S_4$ sample at different magnifications.

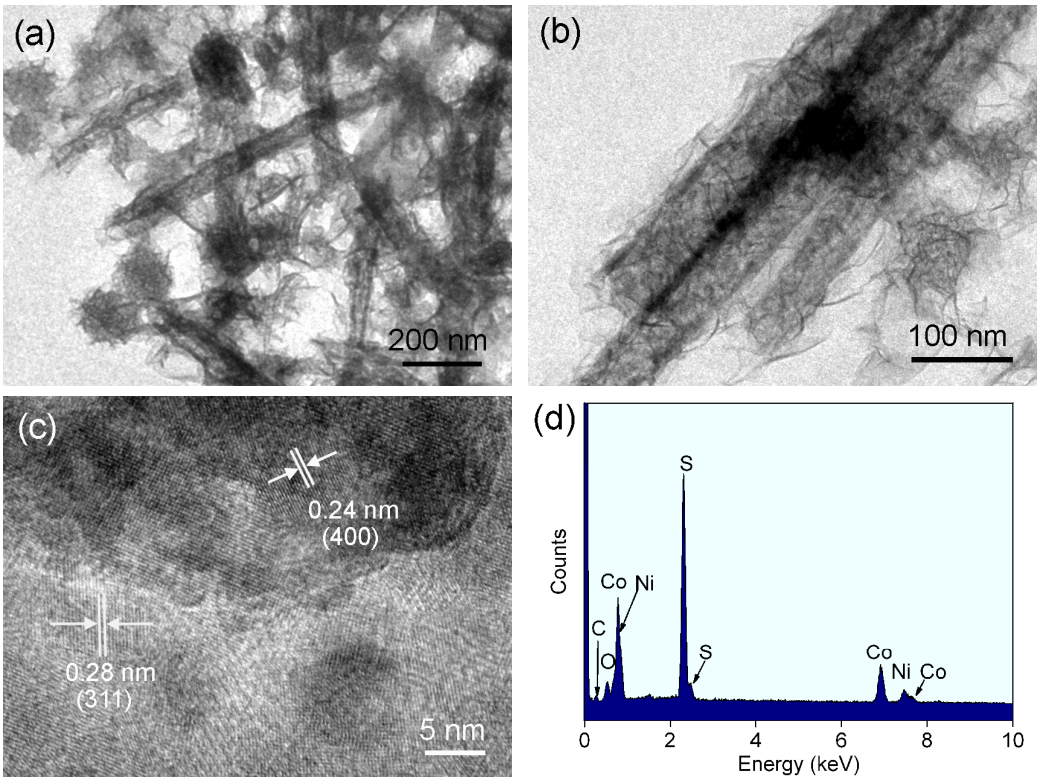

Figure 4. (a,b) TEM images, (c) HRTEM and (d) EDX spectrum of the $NiCo_2S_4$ sample.

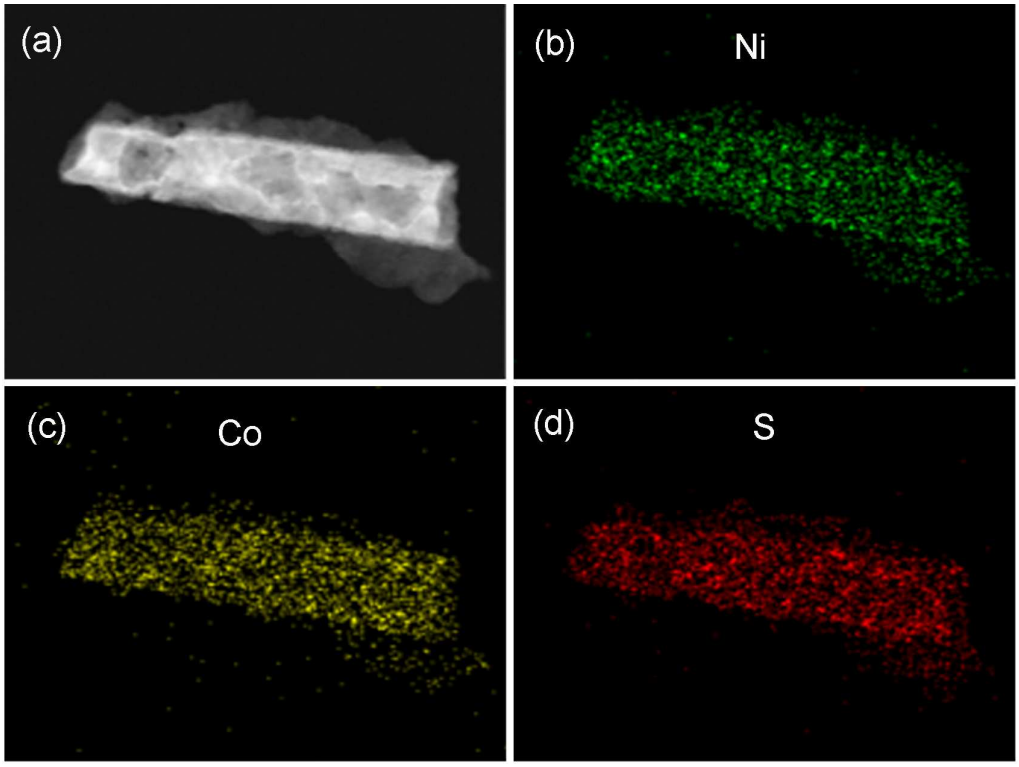

Figure 5. (a) STEM image of the $NiCo_2S_4$ sample; (b–d) elemental mapping images of nickel, cobalt, and sulfur elements.

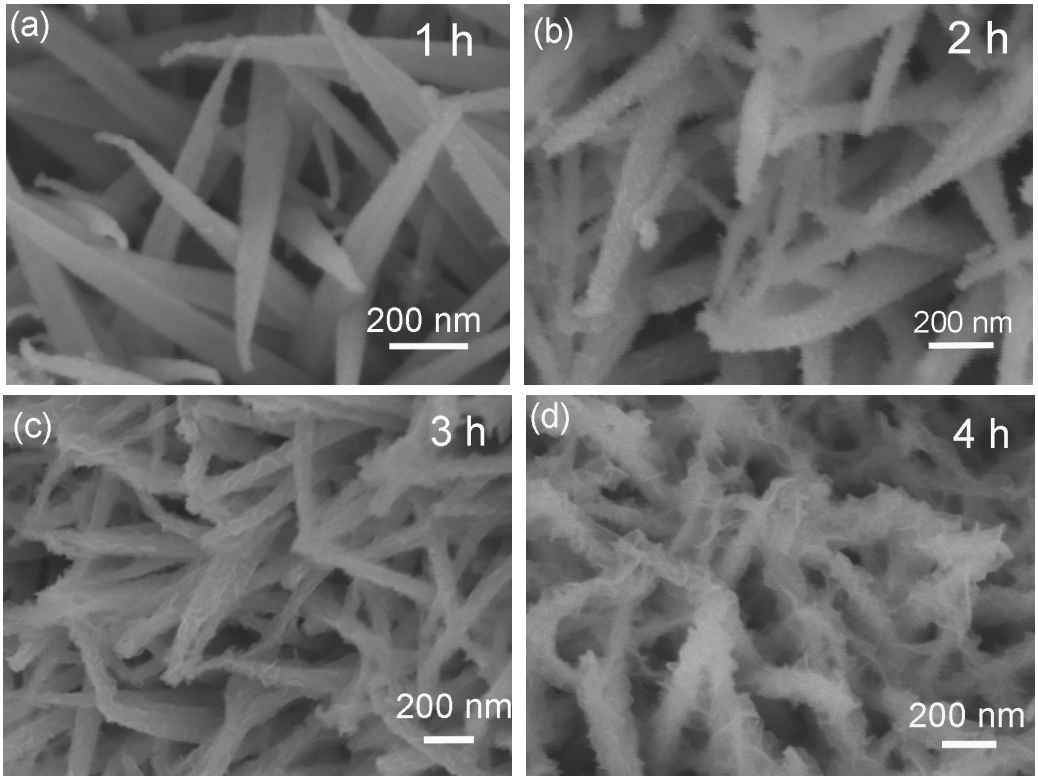

Figure 6. SEM images of $NiCo_2S_4$ sample obtained at 110°C for different reaction time, (a) 1 h, (b) 2 h, (c) 3 h and (d) 4 h.

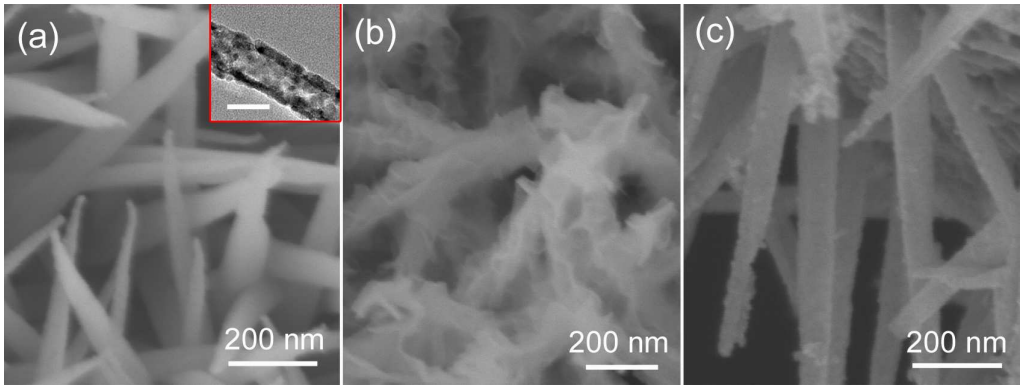

Figure 7. SEM images of $NiCo_2S_4$ samples obtained at (a) 120 °C, (b) 110°C and (c) 100 °C in the second step reaction. Inset in (a) is the corresponding TEM image, scale bar is 50 nm.

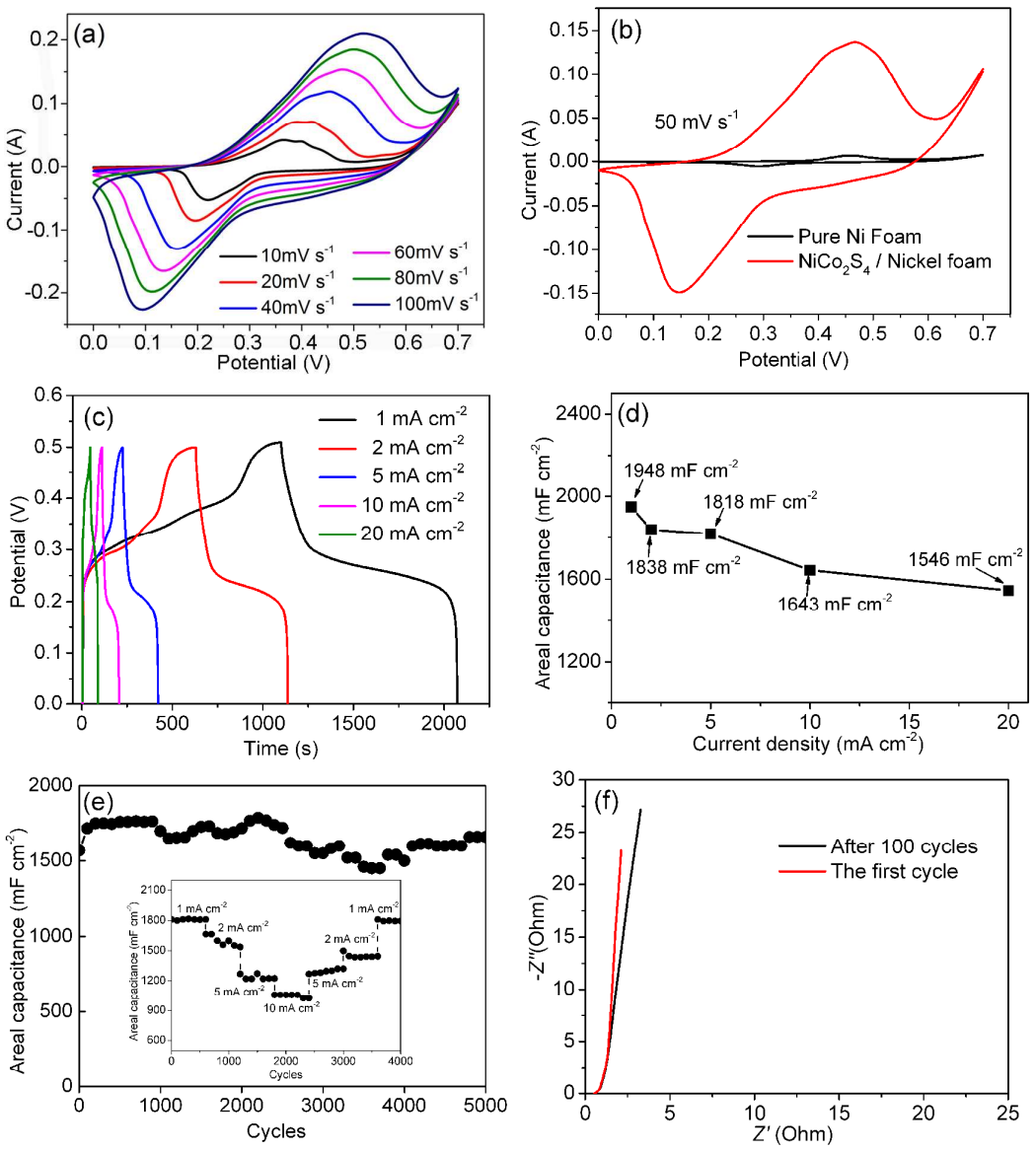

Figure 8. (a) CV curves of $NiCo_2S_4$ electrode at different scan rate; (b) comparative CV curves at 50 mV s^{-1} for $NiCo_2S_4$/Ni foam and pure Ni foam; (c) charge–discharge curves of $NiCo_2S_4$ electrode at different current densities; (d) the specific capacitance as a function of the current densities of the $NiCo_2S_4$ electrode; (e) cycling performances of $NiCo_2S_4$ electrode at 2 mA cm^{-2} for 5000 cycles, inset is the cycling performances at various current densities; (f) Nyquist plots of $NiCo_2S_4$ electrode.

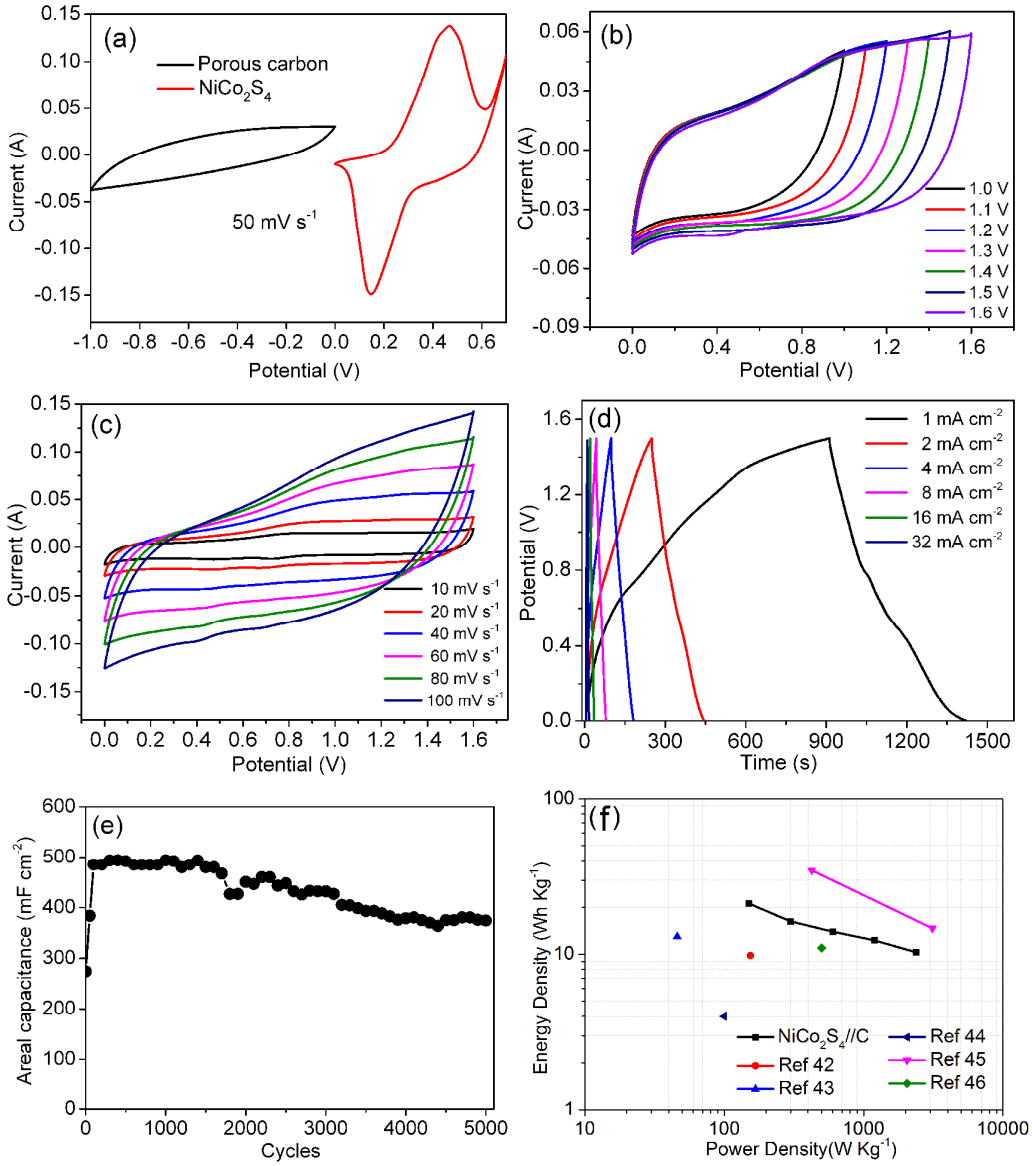

Figure 9. (a) Comparative CV curves of porous carbon and $NiCo_2S_4$ at a scan rate of 50 mV s^{-1} in three-electrode system; (b,c) CV curves of $NiCo_2S_4$//C asymmetric supercapacitor device at different voltage window and different scan rates; (d) charge–discharge curves of $NiCo_2S_4$//C device at different current densities; (e) cycling performances of $NiCo_2S_4$//C asymmetric supercapacitor device; (f) Ragone plot of $NiCo_2S_4$//C device compared to extant literatures.

Graphical Abstract

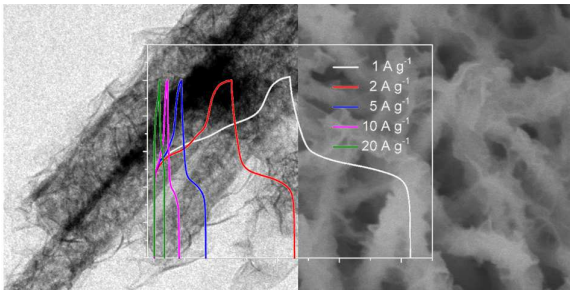

Homogeneous core–shell $NiCo_2S_4$ nanostructure supported on nickel can be applied as high-performance supercapacitor electrode.